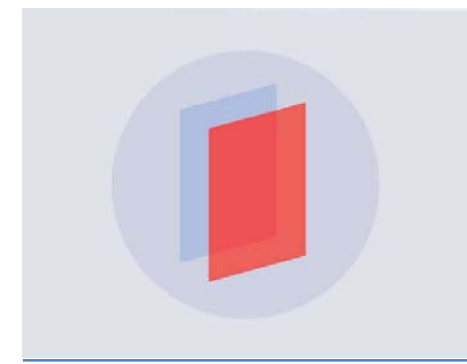


Study of silicon photomultiplier performance in external electric fields

To cite this article: X.L. Sun et al 2018 JINST 13 T09006

View the <u>article online</u> for updates and enhancements.



IOP ebooks™

Bringing you innovative digital publishing with leading voices to create your essential collection of books in STEM research.

Start exploring the collection - download the first chapter of every title for free.



RECEIVED: July 10, 2018 Accepted: September 5, 2018 Published: September 17, 2018

TECHNICAL REPORT

Study of silicon photomultiplier performance in external electric fields

nEXO collaboration

- X.L. Sun, T. Tolba, A. G.F. Cao, A., P. Lv, L.J. Wen, A. Odian, F. Vachon, A. Alamre, J.B. Albert, e G. Anton, f I.J. Arnquist, g I. Badhrees, d,3 P.S. Barbeau, h D. Beck, i V. Belov, f T. Bhatta, F. Bourque, J. P. Brodsky, E. Brown, T. Brunner, A. Burenkov, L. Cao, P. W.R. Cen,^a C. Chambers,^q S.A. Charlebois,^c M. Chiu,^r B. Cleveland,^{s,4} M. Coon,ⁱ M. Côté^c A. Craycraft, W. Cree, d, J. Dalmasson, d, T. Daniels, L. Darroch, S.J. Daugherty, dJ. Daughhetee, k S. Delaquis, b,6 A. Der Mesrobian-Kabakian, s R. DeVoe, t J. Dilling, o Y.Y. Ding, M.J. Dolinski, A. Dragone, J. Echevers, L. Fabris, D. Fairbank, W. Fairbank, J. Farine, S. Feyzbakhsh, P. Fierlinger, R. Fontaine, D. Fudenberg, G. Gallina, G. Giacomini, R. Gornea, do G. Gratta, E.V. Hansen, D. Harris, M. Heffner, E. W. Hoppe, B. J. Hößl f A. House, l P. Hufschmidt, f M. Hughes, z Y. Ito, n,7 A. Iverson, q A. Jamil, aa C. Jessiman, M.J. Jewell, X.S. Jiang, A. Karelin, L.J. Kaufman, b, e D. Kodroff, T. Koffas, d S. Kravitz, t, R. Krücken, A. Kuchenkov, K.S. Kumar, ab Y. Lan, A. Larson, k D.S. Leonard, ac G. Li, b S. Li, b Z. Li, b C. Licciardi, b Y.H. Lin, b R. MacLellan, b T. Michel, fM. Moe, ad B. Mong, D.C. Moore, ad K. Murray, R.J. Newby, Z. Ning, O. Nioya, b. F. Nolet, C. O. Nusair, z K. Odgers, m M. Oriunno, b J.L. Orrell, g G. S. Ortega, g I. Ostrovskiv, z C.T. Overman, S. Parent, A. Piepke, A. Pocar, J.-F. Pratte, D. Qiu, V. Radeka, T. E. Raquzin, T. Rao, S. Rescia, F. Retière, A. Robinson, T. Rossignol, P.C. Rowson, D.
- J. Todd, q T.I. Totev, n R. Tsang, g T. Tsang, r B. Veenstra, d V. Veeraraghavan, z G. Visser, e
- J.-L. Vuilleumier, ae M. Wagenpfeil, Q. Wang, J. Watkins, M. Weber, W. Wei, a

N. Roy, R. Saldanha, S. Sangiorgio, S. Schmidt, J. Schneider, D. Sinclair, d. K. Skarpaas VIII, b A.K. Soma, z G. St-Hilaire, c V. Stekhanov, j T. Stiegler, l M. Tarka, ab,9

U. Wichoski, G. Wrede, S.X. Wu, W.H. Wu, Q. Xia, L. Yang, Y.-R. Yen, O. Zeldovich, J. Zhao, a Y. Zhou p and T. Ziegler f

¹Corresponding author.

²Also at University of Chinese Academy of Sciences, Beijing 100049, China.

³Home institute King Abdulaziz City for Science and Technology, KACST, Riyadh 11442, Saudi Arabia.

⁴Also at SNOLAB, ON P3Y 1N2, Canada.

⁵Now at Canadian Department of National Defense.

⁶Deceased.

⁷Now at JAEA, Ibaraki, Japan.

⁸Now at Lawrence Berkeley National Laboratory, Berkeley, CA 94720, U.S.A.

⁹Now at University of Massachusetts, Amherst, MA 01003, U.S.A.

- ^aInstitute of High Energy Physics, Chinese Academy of Sciences, Beijing 100049, China
- ^bSLAC National Accelerator Laboratory, Menlo Park, CA 94025, U.S.A.
- ^c Université de Sherbrooke, Sherbrooke, Québec J1K 2R1, Canada
- ^dDepartment of Physics, Carleton University, Ottawa, Ontario K1S 5B6, Canada
- ^eDepartment of Physics and CEEM, Indiana University, Bloomington, IN 47405, U.S.A.
- ^f Erlangen Centre for Astroparticle Physics (ECAP), Friedrich-Alexander University Erlangen-Nürnberg, Erlangen 91058, Germany
- ^g Pacific Northwest National Laboratory, Richland, WA 99352, U.S.A.
- ^hDepartment of Physics, Duke University, and Triangle Universities Nuclear Laboratory (TUNL), Durham, NC 27708, U.S.A.
- ⁱPhysics Department, University of Illinois, Urbana-Champaign, IL 61801, U.S.A.
- ^jInstitute for Theoretical and Experimental Physics, Moscow 117218, Russia
- ^kDepartment of Physics, University of South Dakota, Vermillion, SD 57069, U.S.A.
- ¹Lawrence Livermore National Laboratory, Livermore, CA 94550, U.S.A.
- ^mDepartment of Physics, Applied Physics and Astronomy, Rensselaer Polytechnic Institute, Troy, NY 12180, U.S.A.
- ⁿPhysics Department, McGill University, Montréal, Québec H3A 2T8, Canada
- ^oTRIUMF, Vancouver, British Columbia V6T 2A3, Canada
- ^pInstitute of Microelectronics, Chinese Academy of Sciences, Beijing 100029, China
- ^qPhysics Department, Colorado State University, Fort Collins, CO 80523, U.S.A.
- ^rBrookhaven National Laboratory, Upton, NY 11973, U.S.A.
- ^sDepartment of Physics, Laurentian University, Sudbury, Ontario P3E 2C6 Canada
- ^tPhysics Department, Stanford University, Stanford, CA 94305, U.S.A.
- ^uDepartment of Physics and Physical Oceanography, University of North Carolina at Wilmington, Wilmington, NC 28403, U.S.A.
- ^vDepartment of Physics, Drexel University, Philadelphia, PA 19104, U.S.A.
- ^wOak Ridge National Laboratory, Oak Ridge, TN 37831, U.S.A.
- ^xAmherst Center for Fundamental Interactions and Physics Department, University of Massachusetts, Amherst, MA 01003, U.S.A.
- ^yTechnische Universität München, Physikdepartment and Excellence Cluster Universe, Garching 80805, Germany
- ²Department of Physics and Astronomy, University of Alabama, Tuscaloosa, AL 35487, U.S.A.
- aa Department of Physics, Yale University, New Haven, CT 06511, U.S.A.
- ab Department of Physics and Astronomy, Stony Brook University, SUNY, Stony Brook, NY 11794, U.S.A.
- ac IBS Center for Underground Physics, Daejeon 34126, Korea
- ad University of California, Irvine, CA 92697, U.S.A.
- ae LHEP, Albert Einstein Center, University of Bern, Bern CH-3012, Switzerland

E-mail: tolba@ihep.ac.cn, caogf@ihep.ac.cn

ABSTRACT: We report on the performance of silicon photomultiplier (SiPM) light sensors operating in electric field strength up to $30\,\mathrm{kV/cm}$ and at a temperature of 149 K, relative to their performance in the absence of an external electric field. The SiPM devices used in this study show stable gain, photon detection efficiency, and rates of correlated pulses, when exposed to external fields, within the estimated uncertainties. No visible damage to the surface of the devices was caused by the exposure.

KEYWORDS: Cryogenic detectors; Photon detectors for UV, visible and IR photons (solid-state) (PIN diodes, APDs, Si-PMTs, G-APDs, CCDs, EBCCDs, EMCCDs etc.); Double-beta decay detectors; Noble liquid detectors (scintillation, ionization, double-phase)

ArXiv ePrint: 1807.03007

12

14

14

1	Intr	1			
2	2 Instrumentation				
	2.1	The test station	2		
	2.2	The photo-sensors	4		
	2.3	The Data Acquisition (DAQ) system and data collection	5		
3	Resi	6			
	3.1	Pulse finding algorithm and systematic uncertainty	6		
	3.2	Results for data collected in the dark	9		
		3.2.1 Relative gain	9		
		3.2.2 Prompt cross-talk probability	9		
		3.2.3 Delayed correlated noise probability	10		
	3.3	Results for data collected with light	11		

1 Introduction

Conclusions

I-V curve studies

SiPMs visual inspection

Contents

Silicon photomultipliers (SiPMs) are multi-pixel semiconductor devices, with pixels (microcells) arranged on a common silicon substrate [1]. Each microcell is a Geiger-mode avalanche photodiode (GM-APD), working above the breakdown voltage ($U_{\rm bd}$), and a resistor for passive quenching of the breakdown. SiPMs are designed to have high gain (typically $\sim 10^6$), high photon detection efficiency (PDE) [2], excellent time resolution, and wide range spectral response. They can be used to detect light signals at the single photon level and their dark noise rate can be significantly suppressed at low temperatures. Compared with traditional photomultiplier tubes (PMTs), SiPMs are more compact, can be produced with lower radioactivity [3], and do not require high operating voltage. These features make SiPMs very attractive photosensors for low-background, cryogenic applications such as the liquefied noble-element detectors used in dark matter searches and neutrino physics.

The next generation detector of the Enriched Xenon Observatory, nEXO [4, 5], is one such application that intends to use SiPMs as photosensors to detect scintillation light from liquid xenon (peak wavelength at 175 nm [6]). nEXO will use isotopically enriched liquid xenon (LXe) in a time projection chamber (TPC) to search for the neutrinoless double beta decay of ¹³⁶Xe. It has a projected half-life sensitivity of approximately 10²⁸ years [4], covering most of the parameter space corresponding to the inverted neutrino mass hierarchy (assuming the standard mechanism for

the decay and no axial coupling constant quenching). In order to achieve the required collection efficiency and energy resolution, a $\sim 4\,\mathrm{m}^2$ array of SiPMs will be placed on the cylindrical barrel of the TPC outside the field shaping rings. Such an arrangement will expose the individual SiPM devices to different external electric field strengths that depend upon the position of the SiPM along the drift axis of the detector. Preliminary COMSOL [7] electrostatic simulations show that the SiPMs will be exposed to electric fields as high as $20\,\mathrm{kV/cm}$ in regions close to the cathode, with the electric field vector roughly perpendicular to the SiPM front surface.

While it is known that SiPMs are insensitive to external magnetic fields [8], their performance in strong external electric fields has not been extensively studied. The performance of a SiPM can be affected if the external electric field penetrates into the device. For example, if the external field reaches the avalanche region, typically located 100 nm to 500 nm below the semiconductor surface, it can change the breakdown initiation probability of a microcell [9], thus affecting the photodetection efficiency. However, the top contact of each microcell is highly doped silicon, which should shield the inner volume of the microcell from the external fields. A suitable comparison is a Metal-Oxide-Semiconductor (MOS) capacitor [10], in which the electric field is screened either by a depletion or an accumulation region, depending on the semiconductor doping type and field direction. In the depletion regime, the field extends inside the semiconductor for a few nanometers for high doping concentrations (on the order of 10¹⁹ cm⁻³) and hundreds of nanometers for low doping concentrations (< 10¹⁷ cm⁻³). Because the internal structures and doping concentrations of SiPMs are not disclosed by vendors, the penetration depth of external electric fields is difficult to estimate a priori. Thus the field dependence of each type of device needs to be measured experimentally.

Reference [11] demonstrates that at room temperature SiPMs can operate in a 3.2 kV/cm external electric field with no discernible performance change. In this paper, we study the behavior of SiPMs in a cryogenic environment and with electric fields up to 30 kV/cm. This study measures the changes in the SiPM performance parameters, such as gain, correlated noise, and photon detection efficiency.

2 Instrumentation

2.1 The test station

Figure 1 shows a schematic diagram of the cryogenic test station located at the Institute of High Energy Physics (IHEP) in Beijing, China. The inner test chamber is 200 mm in diameter and 340 mm in length. The inner chamber is vacuum-insulated ($\sim 10^{-5}$ mbar) and wrapped with thermal insulation sheets. Although the station is built to run with LXe, it is capable of handling other gases such as Ar and CF₄. The liquid level inside the test chamber is monitored by eight platinum resistance temperature detectors (RTD) placed at specific heights along a calibrated nylon rod.

A schematic of the SiPM test setup is shown in figure 2, with pictures of the assembly and the SiPM devices shown in figure 3. The SiPMs are mounted on a support board and are placed between a high voltage (HV) cathode mesh and a grounded anode.

For accurate vertical positioning of the SiPMs with respect to the cathode, and to ensure that the SiPM-cathode distance is stable during the measurement, 5 mm long nylon spacers were placed between the SiPM support board and the cathode mesh. The thickness of the SiPMs was measured

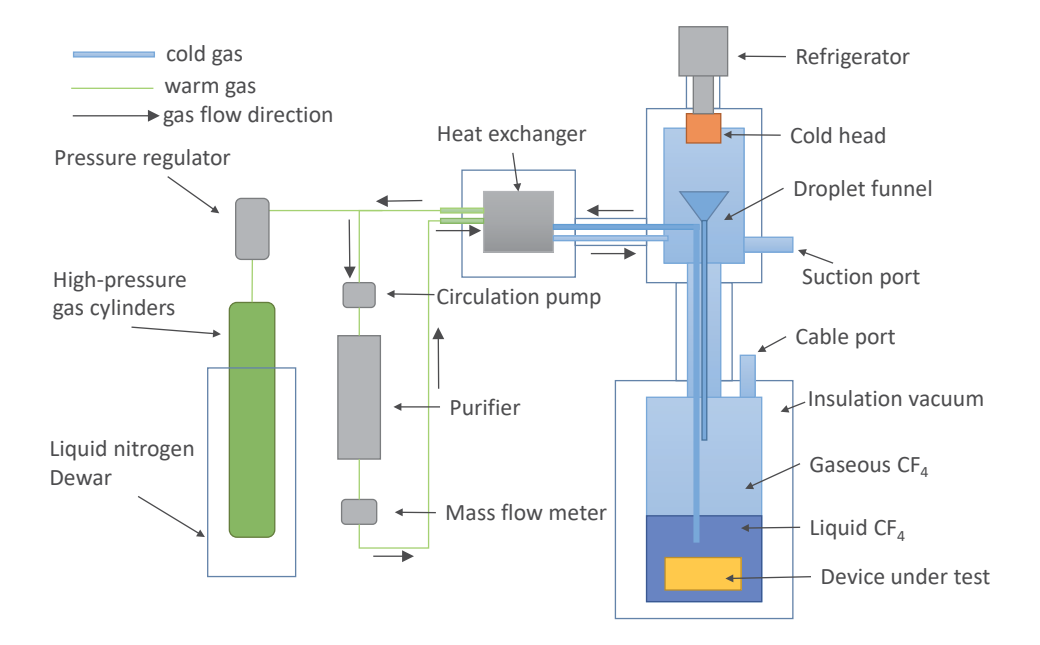


Figure 1. Schematic diagram of the cryogenic test station operated with liquefied CF_4 in these measurements. The arrows indicate the gas flow direction. The cryogen is recovered by cryo-pumping into a high-pressure bottle placed in liquid nitrogen. A plate heat-exchanger is used to improve the efficiency of the recirculation.

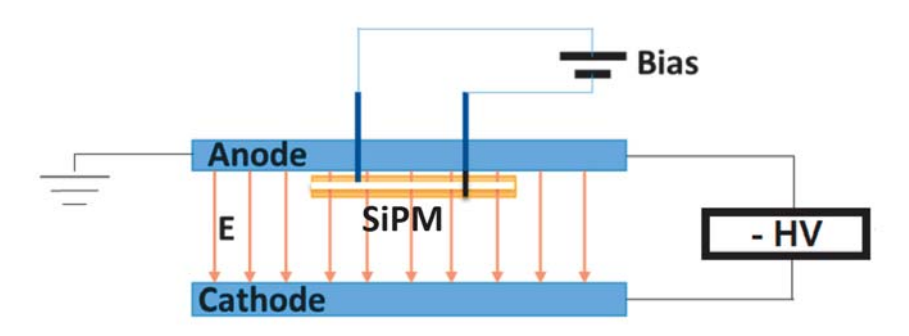


Figure 2. Conceptual design of the SiPM high electric field performance test.

to be 0.5 mm, such that the distance between cathode and SiPM surface was 4.5 mm. The center of the SiPMs support board was aligned to the center of the cathode mesh. The positioning of the SiPMs near the center of the electrode plates and their relatively small size (see table 1) compared to the cathode mesh ($100 \, \text{mm} \times 100 \, \text{mm}$), ensures the uniformity of the external electric field across the surface of the SiPMs. The SiPM bias and signal connections pass through the anode board. The cathode mesh is placed in a nylon frame to avoid discharges between the edge of the cathode plate and the side walls of the inner chamber. All internal components close to the cathode are made of nylon as insulating material. A Spellman high voltage power supply [12] was used to bias the cathode to a maximum of $-20 \, \text{kV}$, with $100 \, \text{V}$ precision. With this setup we have focused on tests where the external fields are perpendicular to, and pointing away from, the device front surface, essentially the nEXO configuration.

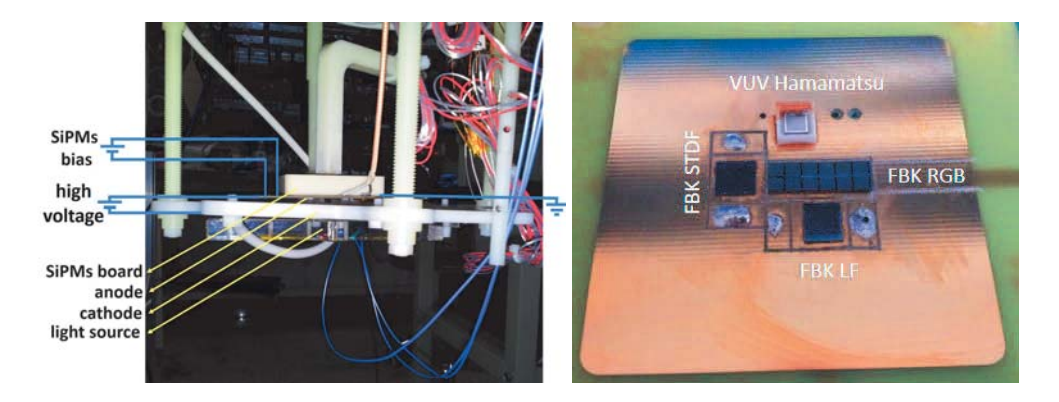


Figure 3. (Left) The assembly of the test setup: SiPMs, cathode and light source in the inner chamber. (Right) The SiPMs used in this study attached to the grounded metallic sheet.

The entire assembly, including the anode and the cathode, is submerged in liquefied CF_4 (LCF₄) at $\sim 149\,\mathrm{K}$ and a pressure of $\sim 1.4\,\mathrm{atm}$. This measurement was carried out in LCF₄ as a practical alternative to LXe. The relevant electrical and thermal properties of LCF₄ are close to those of LXe, as the LCF₄ static dielectric constant (1.614 at 149 K [13]) is only $\sim 15\,\%$ lower than that of LXe (1.874 at 165 K [14]) and its boiling point (145 K at 1 atm) is only $\sim 12\,\%$ lower than that of the LXe (165 K at 1 atm) [15]. Because of the use of CF₄, this study does not explore the characteristics of LXe breakdown relevant to nEXO.

2.2 The photo-sensors

In this study three SiPM devices of interest to the nEXO collaboration were tested. Two devices were from FBK (Fondazione Bruno Kessler) [16]; FBK RGB-HD (FBK-RGB) and FBK Vacuum Ultra Violet (VUV) low field (FBK-LF), and one device was from Hamamatsu [17]; Hamamatsu VUV3 (detailed information for each device is given in table 1). In addition to the two FBK devices listed in table 1, an FBK standard field (FBK-STDF) SiPM was also considered. However, the operating voltage of the FBK-STDF device is significantly reduced at cryogenic temperatures, leading to poor performance, and the results are therefore not reported in this publication.

The FBK devices came as bare dies while the SiPM from Hamamatsu was packaged in a ceramic frame. The FBK-RGB device has the cathode and anode electrodes located on the front and back surfaces, respectively, while they are in the opposite configuration for the FBK-LF SiPM. Thus the two FBK devices are subject to opposite relative orientations of the internal electric field with respect to the external electric field. A thin layer of copper substrate with several isolated pads, attached to a PCB circuit board, was used to mount the devices. The FBK devices were attached to the metal substrate by conductive silver glue, and the cathodes were connected to contacts on isolated pads on the metal substrate by wire bonding. The wire bonds were then protected by UV curable adhesive. The two pins of the Hamamatsu device passed through holes on the substrate. All connections to the preamplifiers were made from the back of the substrate.

Device Dimentions Fill Breakdown Over VUV Page						Packing
Device	Difficutions	I III	Dieakuowii	Ovei	V U V	racking
		factor	voltage	voltage	sensitive	
	[mm ²]	[%]	@149 K	(U_{ov})		
FBK VUV Low Field	5.96 x 5.56	73.0	29.0 V	4.5 V	Yes	Die
FBK RGB-HD [18]	15.30 x 4.95	72.5	24.0 V	3.0 V	No	Die
Hamamatsu VUV3	3.40 x 3.40	50.0	44.0 V	3.5 V	Yes	Ceramic mount

Table 1. Characteristics of the SiPM devices used in this study.

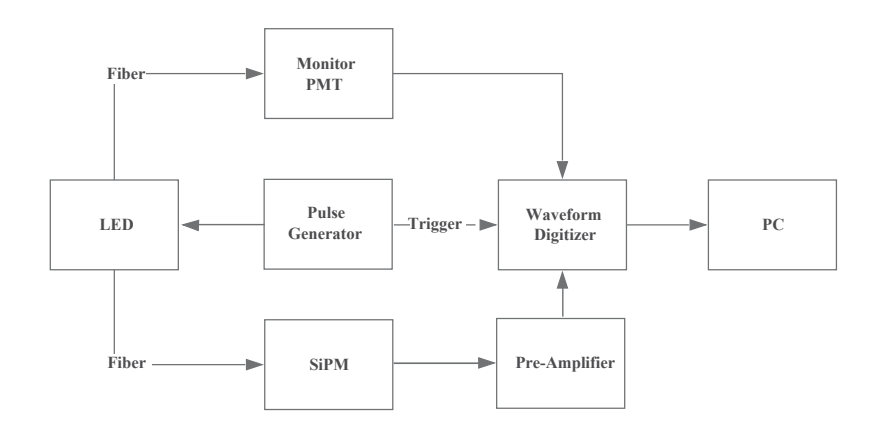


Figure 4. Schematics of the DAQ System for the SiPM measurements with an LED.

2.3 The Data Acquisition (DAQ) system and data collection

Figure 4 shows a schematic diagram of the DAQ system used for the measurement under illumination with LED light. Two different models of preamplifier (which also deliver the bias voltage to the SiPMs) were used in this experiment. For the Hamamatsu VUV3 SiPM we used a commercial Photonique AMP 0604 preamplifier [19], placed outside the chamber at room temperature. For the FBK devices, two custom-made preamplifier were placed inside the chamber in the cold CF₄ gas volume. The two types of preamplifier have very similar properties: current sensitive with 4–10 V supply voltage, signal rise time ~ 5 ns, relatively large bandwidth 10–40 MHz, and gain between 10 and 40. The preamp signals from the SiPMs were digitized by a 4-channel CAEN DT5751 digitizer unit [20] with 10 bit resolution, 1 V dynamic range, and a maximum sampling rate of 1 GHz. The captured pulses were sent to a PC and recorded by custom LabView software [21] for further off-line processing with ROOT [22].

Two sets of data with different illumination conditions were collected at external electric field strengths of 0, 6, 12, 18, 24 and $30\,\text{kV/cm}$. The first data set was collected in the dark with no LED light illumination. In this case, data collected from two different runs were analyzed: one for the Hamamatsu device and one for the FBK devices. The signals from the SiPMs were acquired by setting a threshold on the SiPM output signal amplitude using a leading edge discriminator. The acquisition time window was set to $200\,\mu s$ for the Hamamatsu SiPM aiming to extract more information with the long time window. Later we found that a $1\,\mu s$ time window would have been sufficient for the analysis, so the time window for the FBK devices was chosen to be $1\,\mu s$. The data

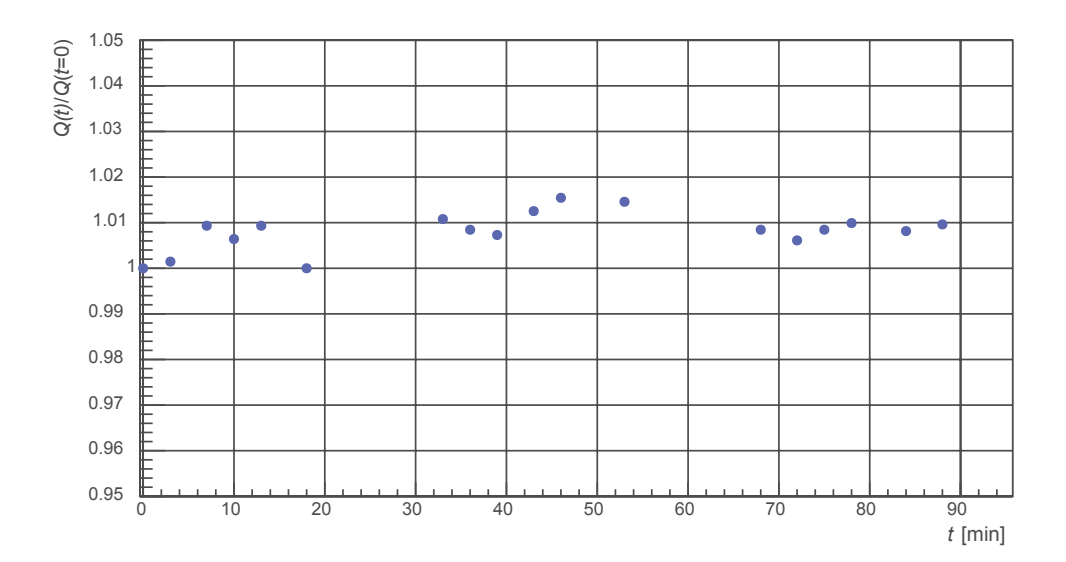


Figure 5. The total charge collected by the monitor PMT as a function of measurement time when illuminated by the LED light source.

were taken over a period of 30 minutes for the Hamamatsu SiPM, with an average trigger rate of $10\,\text{Hz}$. For the FBK SiPMs, the maximum number of events was set to 5×10^5 and 2×10^4 for the FBK-RGB and FBK-LF devices, respectively. For the FBK-LF device, the data collected at $6\,\text{kV/cm}$ were not saved, hence this data point is not present in the following results.

The second data set was collected using a blue (465 nm) LED that was placed outside the test (LCF₄) chamber at room temperature and driven by a pulse generator at $10\,\mathrm{kHz}$ frequency. The light pulse was split into two channels and delivered by optical fibers to the inner test chamber behind the cathode mesh (facing the SiPM) and a PMT outside the chamber used to monitor the stability of the LED light. The PMT used in this test was an ET Enterprises 9364UFLB PMT [23] with a specified gain of 1.3×10^7 . In this data set both the SiPM and the PMT signals were triggered by the pulse generator. The output signals of the monitor PMT were sent directly to the digitizer; no preamplifier was used. The data acquisition program collected the waveforms with a $2\,\mathrm{\mu s}$ readout window and the maximum number of events was set to 5×10^4 . The variation in the output charge of the monitor system (PMT-LED combination) was studied as a function of the measurement time and found to be $\sim 2\,\%$ with respect to that at the beginning of the measurement, as shown in figure 5 (the statistical error bars, much less than $1\,\%$, are not visible on this scale).

For both data sets, all experimental configurations were kept the same throughout the data taking at various external electric fields.

3 Results

3.1 Pulse finding algorithm and systematic uncertainty

The offline analysis first discriminates light signals from noise using a pulse finding algorithm (PFA), then calculates the total charge, Q_{tot} , collected by the light sensors (the SiPMs or the PMT) for each event. The PFA selects signal pulses using a series of cuts. It first sets a lower limit on

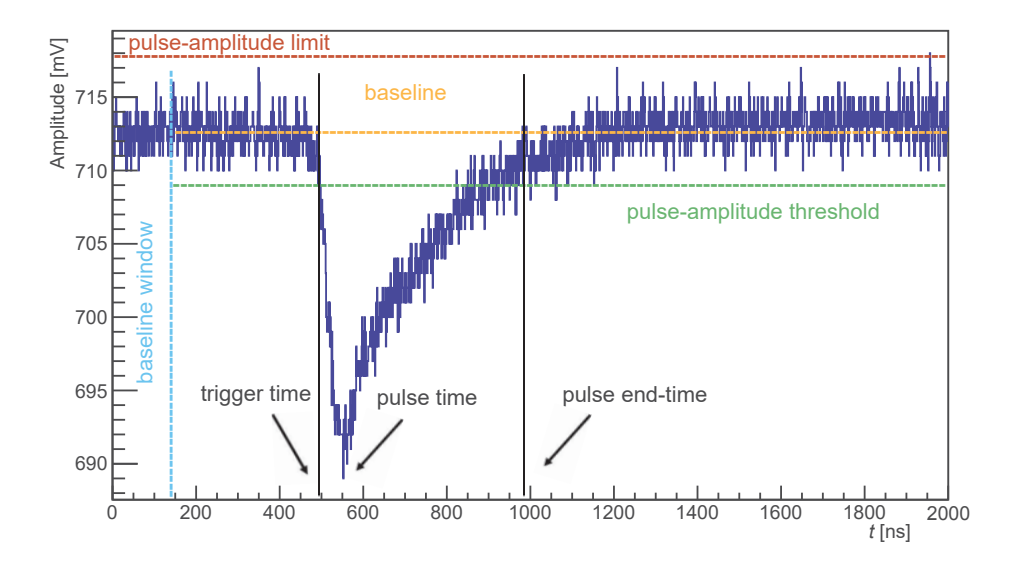


Figure 6. An example of a typical digitized waveform shown together with its baseline, trigger threshold, trigger time and pulse end times, as defined in the text.

the pulse amplitude above the baseline. It then looks at the correlation between the pulse width and the corresponding integrated charge, as a 2D histogram. A ROOT graphical cut is used in this 2D plot to select and exclude the false signals and noise pulses with low charge and/or small width. The signal selection and noise rejection efficiencies of the cuts are measured from the individual spectrum of each cut. Close to 100% of the signals pass the cuts while more than $\sim 95\%$ of noise events are rejected. The total charge for each identified signal is calculated by integrating the total ADC values in the pulse after baseline subtraction. The baseline is defined as the average of the waveform in the time window prior to the trigger ([0, 140-500] ns, depending on the position of the light signal in the waveform for each SiPM). The analysis is repeated for the data collected at different external electric fields. Figure 6 shows an example of a typical waveform along with some of its characteristic features, while figure 7 shows the output charge spectrum for the three SiPMs at $E=18\,\mathrm{kV/cm}$. Each peak above zero in figure 7 corresponds to a quantized number of photoelectrons, p.e., while the few entries around zero are caused by the inefficiency of the PFA noise rejection. These noise events are not included in the following calculations. The multi p.e. peaks are fitted with a sum of independent Gaussian functions to estimate the gain.

Since this study mostly involves relative measurements, systematic effects that are independent of the external electric field cancel out. For the gain measurements, the total uncertainty is dominated by the systematic uncertainty related to changes in electronics pickup from the HV power supply as a function of high voltage. To estimate this uncertainty we measured the FWHM of the baseline variations at different high voltage settings. We found at most $\sim 7\,\%$ deviation, for widths measured at non-zero external electric fields compared to that at zero external field. This baseline noise was then added to simulated signal pulses to estimate its effect on the total charge calculation. This Monte Carlo study indicates that the excess noise pickup can lead to systematic errors in the measurement of the gain by the PFA of up to 1.5 %. The statistical uncertainty for the gain measurement was found to be negligible.

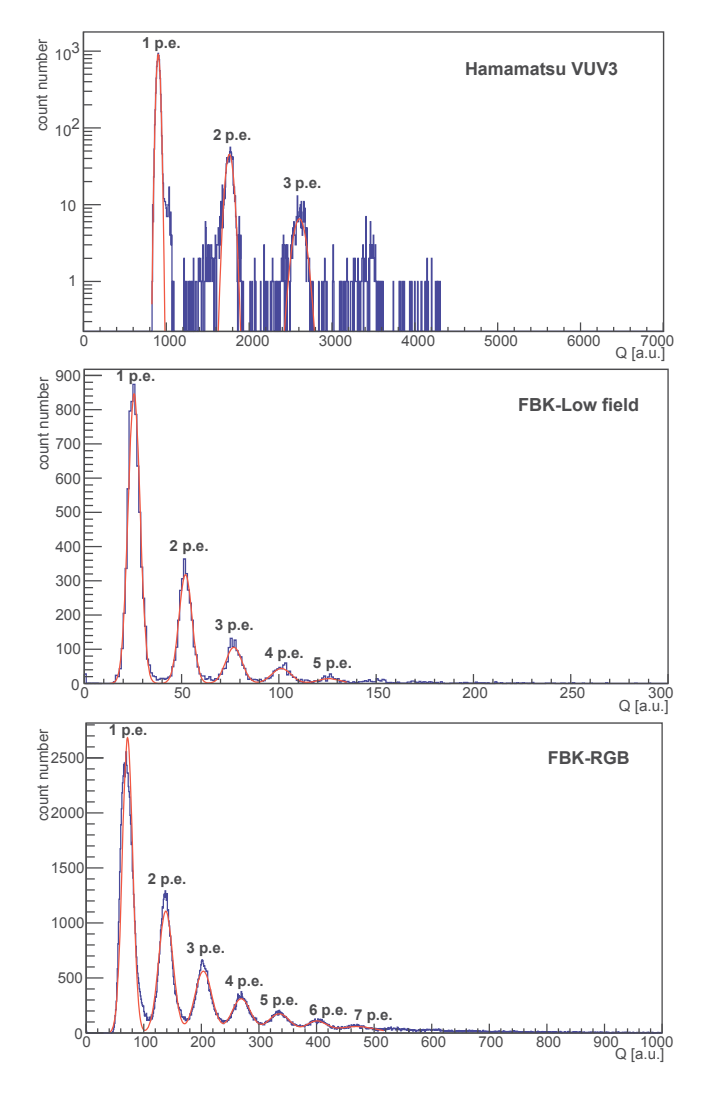


Figure 7. The output charge spectrum of the Hamamatsu VUV3 (top), FBK-LF (middle) and FBK-RGB (bottom) SiPMs in an external electric field of $E = 18 \, \text{kV/cm}$. The multi p.e. peaks are fitted with a sum of independent Gaussian functions (red line). The shoulder on the right side of the single p.e. peak is due to after-pulses.

The correlated noise measurements, on the other hand, are limited by statistical uncertainties, as the following two systematic uncertainties are found to be sub-dominant. The first is interference generated by the high voltage supply. This noise usually appears as symmetrical pulses around the baseline and can be excluded efficiently by setting a limit on the positive amplitude of the waveform in the PFA. A second source of systematic uncertainty is the presence of background light signals due to possible faint discharges in the liquid at high electric fields. Such events would appear as multiple light signals in close time proximity to each other. We measured the presence of such events by looking for additional signals in the first μ s after the trigger, but no such excess of light signals was observed. The total systematic uncertainty is estimated to be below 1 % for the correlated noise

	Table 2. Summary of the most significant error sources to the different parameters studied in this paper.								
Parameter		Dominant error	Value [%]	Source of the uncertainty					
	Relative gain	Systematic	~ 1.5	HV induced baseline noise					
	Prompt cross-talk probability	Statistical	~ 2	Total number of prompt signals					
	Delayed correlated noise probability	Statistical	~ 1.5–4	Counts of the delayed CN signals					

Systematic

~ 2

PMT-LED output stability

Table 2. Summary of the most significant error sources to the different parameters studied in this paper

measurements. Table 2 summarizes the most significant uncertainty sources for each of the studied parameters. While the fits do not show perfect agreement in all regions of the charge spectra for the FBK-RGB device, changing the fit range and the position of the 1.5 p.e. cut had a negligible effect on the estimated parameters, especially the gain and the cross-talk probability.

To account for the uncertainty on the vertical distance between the anode, SiPMs, and cathode surfaces, a 5 % uncertainty in the value of the electric field strength was assumed.

3.2 Results for data collected in the dark

We used the data set collected in the dark to study the relative gain and the stability of the correlated noise at different external electric fields. Because of the large DAQ dead-time, we were not able to make a precise measurement of the dark rate in this study.

3.2.1 Relative gain

Relative PDE

The gain of a SiPM can be defined as the mean number of output electrons in the single p.e. peak [24]. We used the charge distribution of the prompt signal, e.g. in figure 7, to study the relative stability in the gain of the SiPMs at different external electric fields. The mean value of each individual fitted Gaussian is used to estimate the average charge of the corresponding number of photoelectrons, $Q_{\text{n p.e.}(E)}$. The slope of the $Q_{\text{n p.e.}(E)}$ values, when plotted against the number of photoelectrons n, is then used to calculate the average charge of the SiPM single p.e. response at a specific E value, $\bar{Q}(E)$. Thus the stability of the SiPM gain at different electric fields can be assessed by the ratio, η_{Gain} , of the charge amplitude, $\bar{Q}(E)$ (with E=6, 12, 18, 24, 30 kV/cm), to that in the absence of the external field:

$$\eta_{\text{Gain}} = \frac{\bar{Q}(E)}{\bar{Q}(E=0)} \tag{3.1}$$

Figure 8 shows that the relative gain of all SiPMs stays constant as a function of the external electric field, with deviations less than $\sim 5\%$ of the value in the absence of an external electric field, and all variations are consistent with the magnitude of the uncertainties.

3.2.2 Prompt cross-talk probability

Correlated signals are an important source of noise in SiPMs. They are composed of prompt optical cross-talk and delayed after-pulses [2]. The delayed correlated noise probability is discussed in section 3.2.3. The origin of prompt cross-talk can be understood as follows: when undergoing an avalanche, carriers near the p-n junction emit photons, due to the scattering of the accelerated electrons. These photons tend to be at near infrared wavelengths and can travel substantial distances through the device, including to neighboring microcells where they may initiate secondary Geiger

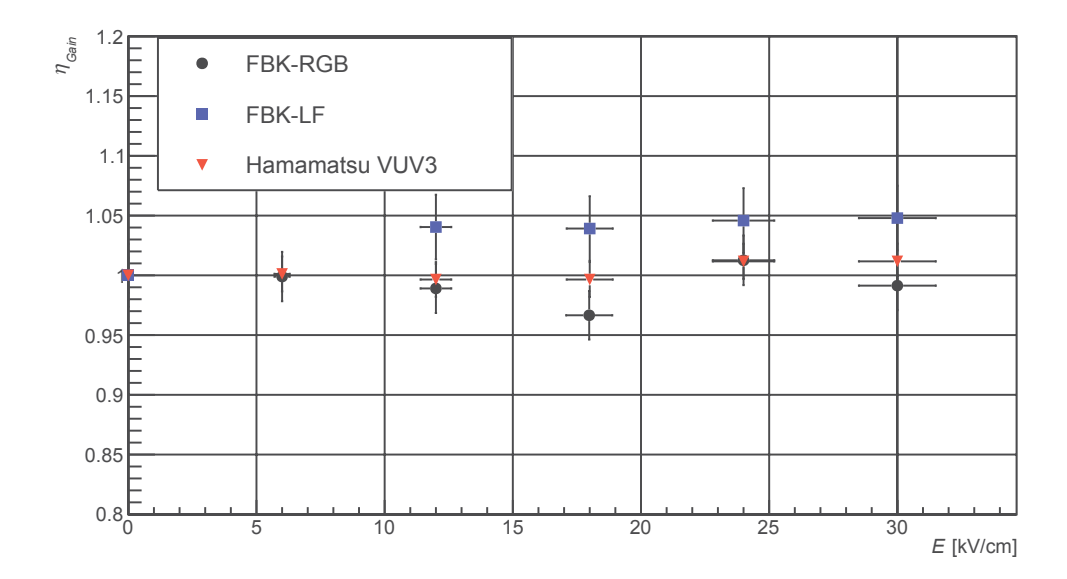


Figure 8. The SiPM relative gain measurements in the dark as a function of external electric field strengths for FBK-RGB (black circles), FBK-LF (blue squares) and Hamamatsu VUV3 (red triangles).

avalanches. As a consequence, a single primary photon may generate signals equivalent to 2 or more photoelectrons [25]. The prompt cross-talk probability, $P_{\rm CT}$, depends on over-voltage, $U_{\rm ov}$, which is the excess bias beyond the breakdown voltage, device-dependent barriers for photons (trenches), and the size of the microcells. Assuming that in the dark the rate of accidental coincidences of multiple pulses triggered by dark noise is negligible at cryogenic temperatures, hence only 1-photoelectron equivalent signals are expected, the probability of prompt cross-talk can be calculated as:

$$P_{\rm CT} = \frac{N_{\rm > 1 \, p.e.}}{N_{\rm total}} \tag{3.2}$$

where $N_{>1\,\mathrm{p.e.}}$ is the number of the prompt signals with a measured charge of at least 1.5 p.e., and N_{total} is the total number of prompt signals above noise. Figure 9 shows $\eta_{P_{\mathrm{CT}}}$, the ratio of $P_{\mathrm{CT}}(E)$ to $P_{\mathrm{CT}}(E=0)$, as a function of the external field. For the FBK devices $\eta_{P_{\mathrm{CT}}}$ does not show a dependence on the external electric fields, within the uncertainty of our measurements. For the Hamamatsu VUV3 there may be a small dependence of $\eta_{P_{\mathrm{CT}}}$ on the external field, but the effect is not significant considering the magnitude of the uncertainties. In all cases possible dependencies on the external field are below 5 %.

3.2.3 Delayed correlated noise probability

Both after-pulsing and delayed cross-talk events originate from an existing pulse. After-pulsing is due to the carriers trapped in silicon defects during the avalanche multiplication, then released later during the recharge phase of the microcell. Delayed cross-talk is generated by a similar mechanism to prompt cross-talk. The difference is that the photons generated during the avalanche process are absorbed in the inactive regions of the neighboring cells instead. It takes some time for the minority charge carriers to diffuse into the active region, causing a delayed signal [24]. In our measurement,

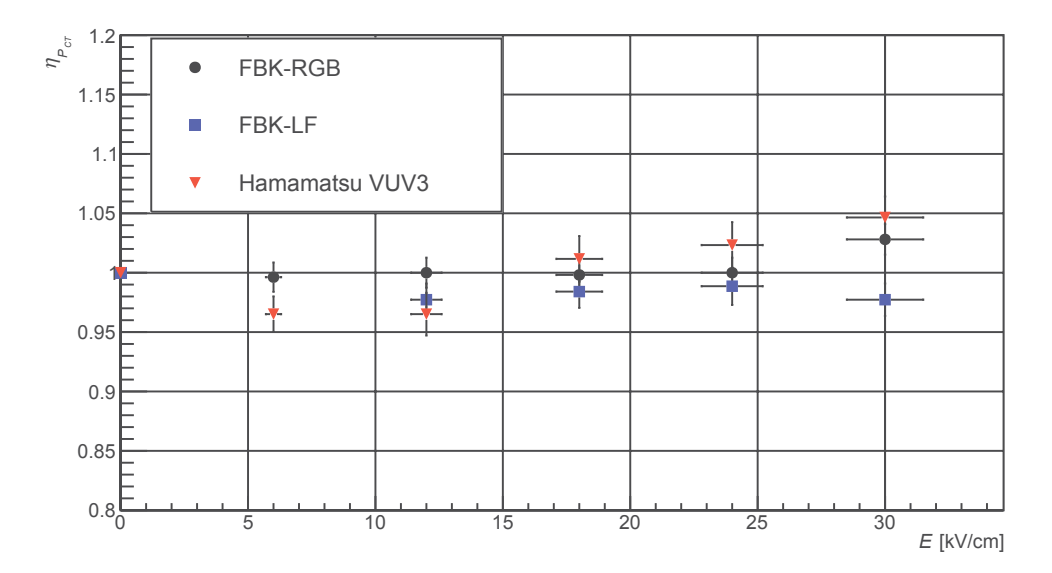


Figure 9. The relative prompt cross-talk, as a function of external electric field values for FBK-RGB (black circles), FBK-LF (blue squares) and Hamamatsu VUV3 (red triangles).

we cannot separate after-pulsing from delayed cross-talk and we count them together as delayed correlated noise.

To estimate the delayed correlated noise probability, $P_{\rm CN}$, we count the number, N, of clearly separated pulses occurring immediately after the primary pulse but within a $0.8\,\mu s$ and a $1\,\mu s$ time interval after the trigger for the FBK devices and the Hamamatsu SiPM, respectively. This time interval, $1\,\mu s$, is sufficiently long for the most of trapped charge to diffuse out. Hence, it has been chosen as the baseline DAQ time window for nEXO. The time window used for the FBK devices is limited by the acquisition window. The primary pulse time window is found to be $\sim 30\, ns$ for the Hamamatsu device and $\sim 20\, ns$ to $55\, ns$ for the FBK devices. $P_{\rm CN}$ is then estimated by normalizing N to the total number of events that contain prompt signals, $N_{\rm prompt}$:

$$P_{\rm CN} = \frac{N}{N_{\rm prompt}} \tag{3.3}$$

At the $U_{\rm ov}$ values listed in table 1, $P_{\rm CN}$ in the absence of an external field is found to be $\sim 9\,\%$, 49 % and 2.2 % for the FBK-RGB, FBK-LF and Hamamatsu VUV3 SiPMs, respectively. Figure 10 shows $\eta_{P_{\rm CN}}$ as a function of the external electric field strength. We observe a constant response with a maximum deviation of $\sim 8\,\%$ compared to the value in the absence of any external electric field, for all three SiPMs tested.

3.3 Results for data collected with light

In this data set the SiPMs are illuminated by a blue LED, as described in section 2.3. The LED signals are sent simultaneously to the SiPMs and a monitor PMT. The ratio, η_{PDE} , of the total SiPM output charge at each HV value, $Q_{\text{total}}(E)$, to that at 0 kV value, $Q_{\text{total}}(E=0)$, is computed as a function of the electric field strength at the SiPM surface:

$$\eta_{\text{PDE}} = \frac{Q_{\text{total}}(E)}{Q_{\text{total}}(E=0)}$$
(3.4)

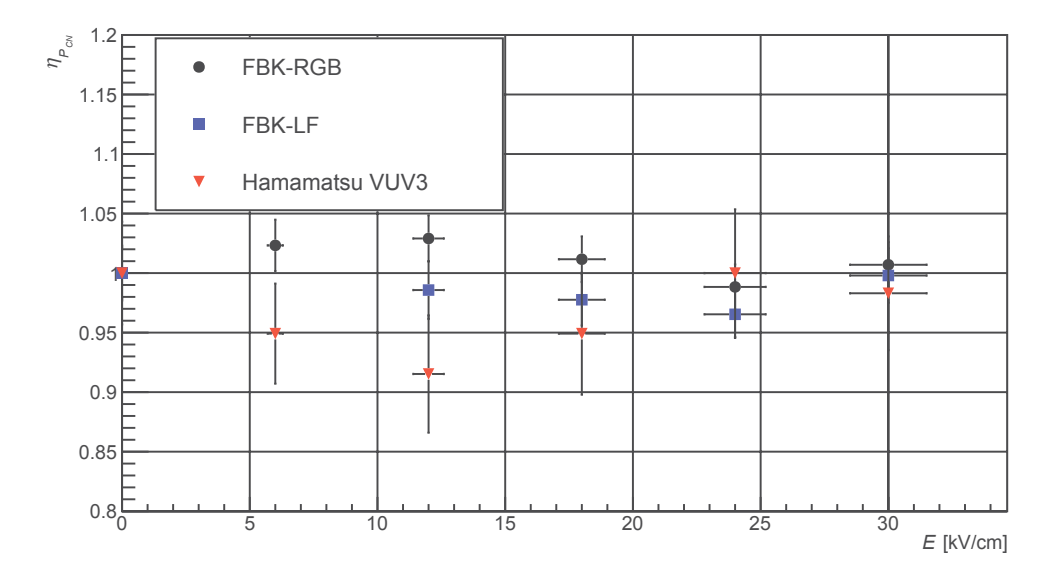


Figure 10. The relative delayed correlated noise as a function of external field values for FBK-RGB (black circles), FBK-LF (blue squares) and Hamamatsu VUV3 (red triangles).

Because the measurements in the dark show that the SiPM gains do not change with the external electric field, we can consider this measurement under LED illumination as a test of the stability of the SiPM photon detection efficiency (PDE) for 465 nm light. The uncertainty in the relative PDE measurement is dominated by the systematics in the stability of the monitor system as discussed in section 2.3. Figure 11 shows η_{PDE} as a function of the external electric field values for the FBK-RGB, FBK-LF, and Hamamatsu VUV3 SiPMs. It can be seen that the SiPMs PDE for 465 nm light does not change with external electric fields, within 5 % deviation compared to that at the absence of the external field.

3.4 I-V curve studies

Because SiPM I-V curves can reveal subtle changes in their characteristics, we measured the I-V curves of each device at different external electric field strength as a cross-check. In this measurement, we connected the anode and cathode of each SiPM to a picoammeter (Keithley 6487 [26]) at $149 \, \text{K}$ and measured its leakage currents as a function of the bias voltage. The bias voltage was incremented in steps of $0.5 \, \text{V}$ up to $8-10 \, \text{V}$ below the breakdown voltage (determined at room temperature), after which the step size was reduced to $0.1 \, \text{V}$ to improve the accuracy of the breakdown voltage determination. This study was repeated twice: in the dark and with the LED light source operating in a continuous mode. The effective resolution of the system is dominated by noise pickup, which is on the order of $100 \, \text{pA}$.

Figure 12 (left column) shows the I-V curves for the three types of SiPMs measured in the dark, while the right column shows the results when the SiPMs are illuminated by the blue LED. The onset of breakdown is clearly visible with LED illumination at about 24 V, 29 V and 44 V for the FBK-RGB, FBK-LF, and Hamamatsu VUV3 SiPMs, respectively. The onset of breakdown is less obvious without illumination because the dark current is very low at 149 K. Within the resolution of the measurement the onset of breakdown does not change with external electric field. The

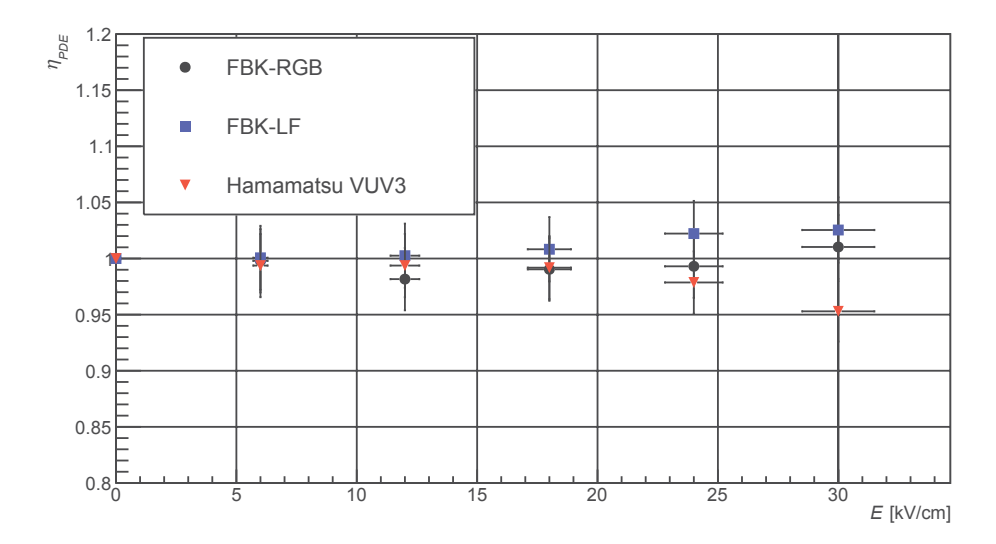


Figure 11. Dependence of the relative charge collected by the SiPMs under 465 nm light illumination as a function of external electric field strength for FBK-RGB (black circles), FBK-LF (blue squares) and Hamamatsu VUV3 (red triangles).

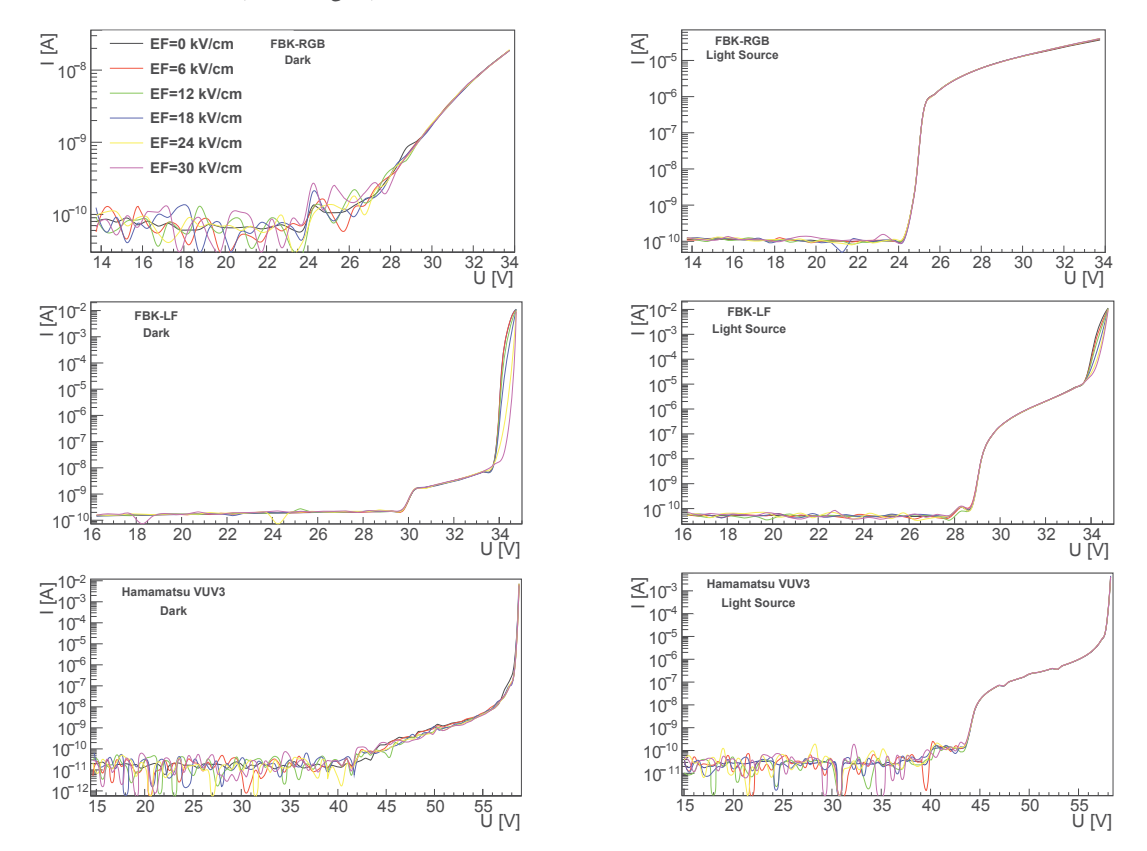


Figure 12. I-V curves for FBK-RGB (top), FBK-LF (middle) and Hamamatsu VUV3 (bottom) SiPMs. Data in the left column are taken in the dark, while data in the right column are taken under continuous illumination with a 465 nm light from a blue LED.

FBK-LF and Hamamatsu VUV3 SiPMs also clearly show a runaway transition, at about 34 V and 57 V respectively. Such a transition is electric field independent for the Hamamatsu device, while it shows a slight dependence on the electric field for the FBK-LF device. The runaway transition occurs when the correlated avalanche rate approaches unity, i.e. when the avalanche production becomes self-sustaining. The operating point of SiPMs is in the span in between the breakdown and runaway voltages. In this condition the mean current scales linearly with the rate of avalanches generated thermally or by photons.

4 SiPMs visual inspection

A visual inspection of the SiPM devices was carried out at the end of the tests using an optical microscope, the Rational VMS-1510F system [27], with magnification power ranging from 20× to 128×. The surfaces of the devices were carefully inspected, and some photographs of specific locations were taken, before and after the high voltage tests. No visible evidence for damage was found on the outer surface of the SiPMs or at the microcell level.

5 Conclusions

We investigated the effect of external electric fields on the operation of several SiPM devices in liquid CF_4 at 149 K. Our experiments show that the performance of these SiPMs, Hamamastu VUV3, FBK-RGB, and FBK-LF, is not affected significantly by external electric fields perpendicular to the surface, up to $30\,\mathrm{kV/cm}$. We measured the I-V curves of the devices, both in the dark and under blue light illumination, confirming that the basic operation parameters of the devices do not change with external electric field. The SiPM devices were also inspected under a microscope and no visible damage was observed.

In summary, our study demonstrates that SiPMs can operate normally in high electric fields at cryogenic temperatures, which bodes well for their use in experiments such as nEXO. In the future we plan to study the long term stability of SiPMs operating in high external electric fields and possible effects due to surface charge build-up.

Acknowledgments

This work has been supported by CAS and ISTCP in China, DOE and NSF in the United States, NSERC, CFI, FRQNT, NRC, and the McDonald Institute (CFREF) in Canada, IBS in South Korea and RFBR in Russia. X.L. Sun was supported, in part, by the Young Scientists Fund of the Chinese National Natural Science Foundation.

References

- [1] G. Bondarenko et al., *Limited Geiger-mode microcell silicon photodiode: New results*, *Nucl. Instrum. Meth.* A 442 (2000) 187.
- [2] nEXO collaboration, A. Jamil et al., *VUV-sensitive Silicon Photomultipliers for Xenon Scintillation Light Detection in nEXO*, arXiv:1806.02220.

- [3] I. Ostrovskiy et al., Characterization Of Silicon Photomultipliers for nEXO, IEEE Trans. Nucl. Sci. 62 (2015) 1825.
- [4] nEXO collaboration, J.B. Albert et al., *Sensitivity and Discovery Potential of nEXO to Neutrinoless Double β Decay*, *Phys. Rev.* C **97** (2018) 065503 [arXiv:1710.05075].
- [5] nEXO collaboration, S.A. Kharusi et al., nEXO Pre-Conceptual Design Report, arXiv:1805.11142.
- [6] K. Fujii et al., *High-Accuracy Measurement of the Emission Spectrum of Liquid Xenon in the Vacuum Ultraviolet Region*, *Nucl. Instrum. Meth.* **A795** (2015) 293.
- [7] COMSOL Multiphysics, https://www.comsol.com.
- [8] R. Hawkes et al., Silicon photomultiplier performance tests in magnetic resonance pulsed fields, *IEEE Nucl. Sci. Symp. Conf. Rec.* **5** (2007) 3400.
- [9] W. Oldham, R. Samuelson and P. Antognetti, *Triggering phenomena in avalanche diodes*, *IEEE Trans. Electron Devices* **19** (1972) 1056.
- [10] S.M. Sze and K.K. Ng, *Physics of semiconductor devices*, John Wiley & Sons (2006).
- [11] B. Godfrey et al., On the Evaluation of Silicon Photomultipliers for Use as Photosensors in Liquid Xenon Detectors, 2018 JINST 13 C03041 [arXiv:1706.05371].
- [12] Spellmanhv, http://www.spellmanhv.com.
- [13] N. Gee and G.R. Freeman, *Relative permittivities of 10 organic liquids as functions of temperature*, *J. Chem. Thermodyn.* **25** (1993) 549.
- [14] R.L. Amey and R.H. Cole, *Dielectric Constants of Liquefied Noble Gases and Methane*, *J. Chem. Phys.* **40** (1964) 146.
- [15] W.M. Haynes, *CRC Handbook of Chemistry and Physics*, 95th edition, CRC Press LLC, Boca Raton (2014–2015).
- [16] Fondazione Bruno Kessler, https://www.fbk.eu.
- [17] Hamamatsu, http://www.hamamatsu.com.
- [18] N. Serra et al., *Characterization of New FBK SiPM Technology for Visible Light Detection*, 2013 *JINST* **8** P03019.
- [19] Photonique SA, AMP-0604 and AMP-0611 Amplifiers Data Sheet, http://www.photonique.ch/.
- [20] CAEN, DT5751 Digitizer Data Sheet, http://www.caen.it.
- [21] National Instruments, Labview, http://www.ni.com/labview.
- [22] R. Brun and F. Rademakers, *ROOT: An object oriented data analysis framework, Nucl. Instrum. Meth.* **A 389** (1997) 81.
- [23] ET Enterprises, https://my.et-enterprises.com/search?search-source=PMT&q=9364U.
- [24] AdvanSiD, Application note: Introduction to SiPMs, http://advansid.com.
- [25] SensL, Technical Note: Introduction to SiPM, http://www.sensl.com.
- [26] Keithley, http://www.keithley.com.
- [27] Rational Precision Instrument Co. Ltd., http://www.rational-en.com/Productshow-71-443.html.